



THE UNIVERSITY *of* EDINBURGH

Edinburgh Research Explorer

Conservation of the structural and functional architecture of encapsulated ferritins in bacteria and archaea

Citation for published version:

He, D, Piergentili, C, Ross, J, Tarrant, E, Tuck, LR, Mackay, CL, Mciver, Z, Waldron, KJ, Clarke, DJ & Marles-wright, J 2019, 'Conservation of the structural and functional architecture of encapsulated ferritins in bacteria and archaea', *Biochemical Journal*, vol. 476, no. 6, pp. 975-989.
<https://doi.org/10.1042/BCJ20180922>

Digital Object Identifier (DOI):

[10.1042/BCJ20180922](https://doi.org/10.1042/BCJ20180922)

Link:

[Link to publication record in Edinburgh Research Explorer](#)

Document Version:

Peer reviewed version

Published In:

Biochemical Journal

General rights

Copyright for the publications made accessible via the Edinburgh Research Explorer is retained by the author(s) and / or other copyright owners and it is a condition of accessing these publications that users recognise and abide by the legal requirements associated with these rights.

Take down policy

The University of Edinburgh has made every reasonable effort to ensure that Edinburgh Research Explorer content complies with UK legislation. If you believe that the public display of this file breaches copyright please contact openaccess@ed.ac.uk providing details, and we will remove access to the work immediately and investigate your claim.



Conservation of the structural and functional architecture of encapsulated ferritins in bacteria and archaea

Didi He^{1,*,*}, Cecilia Piergentili^{2,*}, Jennifer Ross^{3,*}, Emma Tarrant⁴, Laura R. Tuck¹, C. Logan Mackay³, Zak McIver², Kevin J. Waldron⁴, David J. Clarke^{3*}, Jon Marles-Wright^{2*},

¹Institute of Quantitative Biology, Biochemistry and Biotechnology, School of Biological Sciences, The University of Edinburgh, Max Born Crescent, Edinburgh, EH9 3BF; ²School of Natural and Environmental Sciences, Newcastle University. Newcastle upon Tyne, NE1 7RU; ³EaStCHEM School of Chemistry, The University of Edinburgh, Joseph Black Building, David Brewster Road, Edinburgh, Scotland, EH9 3FJ; ⁴Institute for Cell and Molecular Biosciences, Newcastle University, Newcastle upon Tyne, NE2 4HH.

**Current address: Structural Genomics Consortium, University of Oxford, Old Road Campus Research Building, Roosevelt Drive, Oxford, OX3 7DQ*

Running title: Structure and function of EncFtn homologues

* These authors contributed equally to this work

* To whom correspondence should be addressed:

Jon Marles-Wright, +44(0)191 208 4855, Jon.marles-wright1@ncl.ac.uk;

David J. Clarke, +44(0)131 650 4808, Dave.clarke@ed.ac.uk.

KEYWORDS: *encapsulin, encapsulated ferritin, ferritin, ferroxidase, mass spectrometry (MS), metalloprotein, protein assembly, Pyrococcus furiosus, Haliangium ochraceum, X-ray crystallography*

26 **Abstract**

27 Ferritins are a large family of intracellular proteins that protect the cell from oxidative stress by
28 catalytically converting Fe(II) into less toxic Fe(III) and storing iron minerals within their core.
29 Encapsulated ferritins (EncFtn) are a sub-family of ferritin-like proteins, which are widely distributed
30 in all bacterial and archaeal phyla. The recently characterized *Rhodospirillum rubrum* EncFtn
31 displays an unusual structure when compared to classical ferritins, with an open decameric structure
32 that is enzymatically active, but unable to store iron. This EncFtn must be associated with an
33 encapsulin nanocage in order to act as an iron store. Given the wide distribution of the EncFtn family
34 in organisms with diverse environmental niches, a question arises as to whether this unusual
35 structure is conserved across the family. Here, we characterize EncFtn proteins from the
36 halophile *Haliangium ochraceum* and the thermophile *Pyrococcus furiosus*, which show the
37 conserved annular pentamer of dimers topology. Key structural differences are apparent between
38 the homologues, particularly in the centre of the ring and the secondary metal binding site, which is
39 not conserved across the homologues. Solution and native mass spectrometry analyses highlight
40 that the stability of the protein quaternary structure differs between EncFtn proteins from different
41 species. The ferroxidase activity of EncFtn proteins was confirmed, and we show that while the
42 quaternary structure around the ferroxidase centre is distinct to classical ferritins, the ferroxidase
43 activity is still inhibited by Zn(II). Our results highlight the common structural organization and activity
44 of EncFtn proteins, despite diverse host environments and contexts within encapsulins.

45

46 **Introduction**

47 The encapsulated ferritins (**EncFtn**) are recently described members of the ferritin superfamily [1–
48 3]. These proteins are sequestered within encapsulin nanocompartments, and the two proteins act
49 in concert to provide an iron storage system with a much greater capacity than the classical ferritins
50 and DNA-binding Protein from Starved cells (DPS) nanocages [3,4]. Genes encoding encapsulin-
51 associated ferritins have been identified in a wide range of bacterial and archaeal species that inhabit
52 diverse ecological niches from ponds, streams (*Rhodospirillum rubrum*), and coastal seas
53 (*Haliangium ochraceum*), to abyssal ocean vents (*Pyrococcus furiosus*) [5].

54 The *R. rubrum* EncFtn was the first protein in its family to be structurally and biochemically
55 characterized; it has a fold with two antiparallel alpha-helices that adopts an annular-decamer
56 quaternary structure, assembled as a pentamer of dimers [1]. The subunits dimerize through metal-
57 mediated contacts to reconstitute the four-helix ferritin fold with a functional ferroxidase centre [6,7].
58 While the EncFtn protein displays ferroxidase activity, it is not capable of storing iron in the same
59 way as other ferritins due to its open architecture and the lack of an enclosed cavity for iron
60 mineralization [8,9]; therefore, EncFtn family proteins must be localized to the interior of an
61 encapsulin nanocage for efficient iron storage [1,3,5]. Localization to encapsulin nanocages is
62 mediated by a short encapsulation sequence, which is usually appended to the C-terminus of the
63 EncFtn protein chain [1,3,5,10]; addition of this sequence to heterologous proteins is sufficient to
64 direct them to the lumen of encapsulins [11,12].

65 The encapsulin protein family is structurally related to the HK97 bacteriophage shell protein and they
66 form icosahedral nanocages of between 25 and 35 nm in diameter. Pores are formed at the
67 icosahedral symmetry axes between subunits to allow substrate access to encapsulated enzyme
68 cargoes [3,5,10,13]. The *R. rubrum* encapsulin was shown to associate with over 2000 iron ions per
69 capsid, while being catalytically inactive; and, in concert with EncFtn, capable of mineralizing and
70 storing more than four times as much iron as a classical ferritin nanocage [1]. Given the wide
71 distribution of encapsulin proteins across bacterial and archaeal phyla, and the conservation of the
72 EncFtn proteins in 20 % of all phyla with encapsulin genes, we investigated the structure and activity
73 of EncFtn proteins from the halophilic Proteobacterium *H. ochraceum* and the EncFtn-fusion from

74 the Euryarchaeota *P. furiosus*, to determine whether the structural and functional organization seen
75 in the *R. rubrum* EncFtn is conserved within its phylum and between domains and environmental
76 niches.

77 Here we report the structural and biochemical characterization of members of the EncFtn family from
78 *H. ochraceum* and *P. furiosus*. Both proteins adopt similar topology to the *R. rubrum* EncFtn and
79 assemble as annular decamers formed from pentamers of dimers, with ferroxidase centres located
80 at one of the dimer interfaces. The ferroxidase activities of the proteins are comparable, and they
81 show similar levels of inhibition by the competing metal ion zinc. These data show that the structural
82 and biochemical features of encapsulated ferritins are conserved across different environmental
83 niches and phyla with particular adaptations for thermal stability in thermophilic microorganisms.

84

85 **Materials and Methods**

86 *Cloning expression and purification of EncFtn and EncFtn homologues*

87 Recombinant encapsulated ferritin from *Rhodospirillum rubrum* was produced as described
88 previously [1]. DNA fragments encoding truncated versions of the encapsulated ferritins from
89 *Haliangium ochraceum* (Hoch_3836₁₋₉₈) (Uniprot: D0LZ73_HALO1) and *Pyrococcus furiosus*
90 (Pfc_01575₁₋₉₉) (Uniprot: I6U7J4_9EURY) were produced as double-stranded gBlocks (IDT) and
91 codon optimized for expression in *E. coli*, with restriction endonuclease sites for insertion into pET-
92 28a (Pfc_05157₁₋₉₉) or a modified pET-28 vector with CIDAR MoClo [14] Golden Gate cloning sites
93 (Hoch_3836₁₋₉₈). Untagged and His-tagged variants were produced for both proteins in this way. A
94 StreptII-tagged variant of each protein was produced by assembly of the EncFtn gBlock into a CIDAR
95 MoClo destination vector with a custom T7 promoter and StreptII-tag terminator part. Sequences of
96 primers and gBlocks used in this study are shown in Tables S1 and S2 respectively, and the
97 sequences of expressed proteins are shown in Table S3. The expression plasmids were transformed
98 into *E. coli* BL21(DE3) cells and a single colony was grown overnight at 37 °C in 100 ml LB medium,
99 supplemented with 35 µg/ml kanamycin, with shaking at 180 rpm. The cells were sub-cultured into
100 1 L of LB or M9 minimal medium, grown until OD₆₀₀=0.6, and protein production was induced with
101 1 mM IPTG, the temperature was reduced to 18 °C and cells were incubated for a further 18 hours.
102 Cells were harvested by centrifugation at 4,000 × *g* and washed with PBS. Cell-free extract was
103 produced by resuspending cells in 10 x v/w Buffer A (50 mM Tris-HCl, pH 8.0) and sonicated on ice
104 for 5 minutes with 30 s on/off cycle at 60 watts power output. The lysate was cleared by centrifugation
105 at 35,000 × *g* and filtered with a 0.45 µm syringe filter. Untagged recombinant proteins were purified
106 from cell-free extract by anion exchange using HiPrep Q sepharose fast-flow 16/10 column (GE
107 Healthcare) equilibrated with Buffer A. Cell free extract was applied to the column and unbound
108 proteins were washed off with 10 column volumes of Buffer A. Proteins were eluted with a linear
109 gradient of Buffer B (50 mM Tris-HCl, pH 8.0, 1 M NaCl) over 20 column volumes and fractions
110 collected.
111 His-tagged proteins were purified by resuspending cells in 10 x (v/w) Buffer HisA (50 mM Tris-HCl,
112 pH 8.0, 500 mM NaCl, 50 mM imidazole) before sonication and clarification as above. Clarified cell

113 lysate was applied to a 5 ml HisTrap FF column (GE Healthcare) and unbound proteins were washed
114 off with 10 column volumes of Buffer HisA. A step-gradient of 50 % and 100 % Buffer HisB (50 mM
115 Tris-HCl, pH 8.0, 500 mM NaCl, 500 mM imidazole) was used to elute His-tagged proteins.

116 Fractions of Q sepharose or His-trap eluent containing the protein of interest, as identified by 15 %
117 (w/v) SDS-PAGE, were subjected to size-exclusion chromatography using an S200 16/60 column,
118 previously calibrated with LMW/HMW calibration kits (GE Healthcare) (Fig. S1) and equilibrated with
119 Buffer GF (50 mM Tris-HCl, pH 8.0, 150 mM NaCl).

120 StrepII-tagged proteins were purified by suspending cells in 10 x (v/w) Buffer W (100 mM Tris pH
121 8.0, 150 mM NaCl) before sonication and clarification as described above. Cell lysate was applied
122 to Strep-Trap HP column (GE Healthcare), prepared as suggested by the manufacturer, and
123 unbound proteins were washed off by applying 5 column volumes of Buffer W. Strep-tagged proteins
124 were eluted by Buffer E (100 mM Tris pH 8.0, 150 mM NaCl, 2.5 mM desthiobiotin). Eluted protein
125 was buffer-exchanged to Buffer GF by centrifugal concentrator Vivaspın Turbo (Sartorius, 10 kDa
126 MWCO) to remove desthiobiotin.

127 ***Protein quantification***

128 Purified protein concentration was determined by colorimetric technique using the Pierce™ BCA
129 protein assay kit following manufacturer specifications for the standard Test-tube procedure at 37
130 °C. Diluted bovine serum albumin (BSA) standards were prepared in GF buffer. Fig. S2A/B show
131 colour response curves prepared for His-tagged or Strep-tagged protein quantification, respectively.
132 Protein samples absorbance at 562 nm (average of 3 experimental replicates) are listed in Table
133 S4.

134 ***Ferroxidase assays***

135 Ferroxidase activity of the enzymes was tested by following the formation of Fe(III) species by UV-
136 visible spectroscopy at 20 °C, as previously described [1]. Oxygen-free aliquots of Fe(II) (1 mM)
137 were prepared by dissolving FeSO₄·7H₂O in 0.1 % (v/v) HCl under anaerobic conditions. Purified
138 proteins (decameric fraction) were diluted anaerobically to the final concentration of 10 μM monomer
139 in Buffer H (10 mM HEPES pH 8.0, 150 mM NaCl). Protein and Fe(II) samples were added to a

140 quartz cuvette (Hellma) under aerobic conditions at the final concentration of 10 and 50 μM ,
141 respectively. Absorbance at 315 nm was monitored every second over 1500 s using a UV-visible
142 spectrophotometer (Perkin Elmer Lambda 35) using the provided TimeDrive software. A negative
143 control was performed by monitoring the progress curve at A_{315} of Fe(II) salt sample in the absence
144 of protein. Data presented here are the mean of three technical replicates of time zero-subtracted
145 progress curves with standard deviations calculated from the mean.

146 *Zinc inhibition of ferroxidase activity*

147 In order to test enzyme selectivity toward Fe(II), the ferroxidase assay was carried out as previously
148 described [1], in the presence of $\text{FeSO}_4 \cdot 7\text{H}_2\text{O}$ (50 μM) and various concentrations of $\text{ZnSO}_4 \cdot 2\text{H}_2\text{O}$.
149 The A_{315} nm progress curve of protein mixed with the highest concentration of Zn(II) used in the
150 assay (100 μM) was also monitored as a negative control.

151 *Protein Crystallography*

152 Hoch_EncFtn and Pfc_EncFtn were concentrated to 10 mg/ml using a 10 kDa MWCO centrifugal
153 concentrator (Vivaspin) and subjected to sitting drop vapor diffusion crystallization using 70 μl well
154 solution and drops of 100 nl protein, plus 100 nl well solution. Crystals of Hoch_EncFtn grew in well
155 solution containing 0.2 M NaCl, 0.1 M Bis-Tris, pH 5.5, 20 % (w/v) PEG 3350; and crystals of
156 Pfc_EncFtn were found in a condition containing 0.2 M $\text{LiSO}_4 \cdot \text{H}_2\text{O}$, 20 % (w/v) PEG 3350. Crystals
157 were harvested using a LithoLoop (Molecular Dimensions Limited), transferred to a cryoprotection
158 solution of well solution supplemented with 20 % (v/v) PEG 200 and flash cooled in liquid nitrogen.
159 Diffraction data were collected at Diamond Light Source at 100 K using a Pilatus 6M detector. Images
160 were integrated and scaled using XDS [15]; the correct crystallographic symmetry group was
161 confirmed with Pointless [16] and reflections were merged with Aimless [17]. The data were phased
162 by molecular replacement using Phaser, with a decamer of Rru_EncFtn (PDB ID: 5DA5) used as the
163 search model [1]. This has 58 and 22 % sequence identity to the Hoch_EncFtn and Pfc_EncFtn
164 respectively. The sequences were aligned with the 5DA5 protein sequence using ClustalOmega and
165 the alignment was used to edit the search model to match the target sequence using CHAINSAW
166 [18]. The crystallographic models were rebuilt using phenix.autobuild [19] and subsequently refined

167 using phenix.refine [20] with cycles of manual model building in Coot [21]. The model quality was
168 assessed using MolProbity [22]. All structural figures were generated using PyMOL
169 (www.pymol.org). X-ray data collection and refinement statistics are shown in Table 1.

170 ***Sequence alignment and depiction***

171 The protein sequences for Hoch_3836 and the encapsulated ferritin domain of Pfc_05175 were
172 aligned against Rru_A0973 using Clustal Omega [23] and rendered using ESPrnt 3.0 [24].

173 ***Mass spectrometry***

174 All mass spectrometry (MS) experiments were performed on a Synapt G2 ion-mobility equipped Q-
175 ToF instrument (Waters Corp., Manchester, UK). LC-MS experiments were performed using an
176 Acquity UPLC equipped with a reverse phase C4 Aeris Widepore 50 × 2.1 mm HPLC column
177 (Phenomenex, CA, USA) and a gradient of 5–95% acetonitrile (0.1% formic acid) over 10 minutes
178 was employed. For LC-MS, samples were typically analysed at 5 µM, and data analysis was
179 performed using MassLynx v4.1 and MaxEnt deconvolution. For native MS analysis, all protein
180 samples were buffer exchanged into 100 mM ammonium acetate (pH 8.0, or pH 5.0) using Micro
181 Biospin Chromatography Columns (Bio-Rad, UK) prior to analysis and the resulting protein samples
182 were analysed at a typical final concentration of ~5 µM (oligomer concentration). For native MS
183 ionization, nano-ESI was employed using a nanomate nanoelectrospray infusion robot (Advion
184 Biosciences, Ithaca, NY). Instrument parameters were tuned to preserve non-covalent protein
185 complexes and were consistent for the analysis of all protein homologues. After the native MS
186 optimization, parameters were: nanoelectrospray voltage 1.60 kV; sample cone 100 V; extractor
187 cone 0 V; trap collision voltage 4 V; source temperature 60 °C; and source backing pressure 6.0
188 mbar.

189 ***ICP-MS***

190 Inductively coupled plasma mass spectrometry experiments were performed on samples of Rru_His,
191 Hoch_His, and Pfc_His from size-exclusion chromatography experiments and Rru_StrepII,
192 Hoch_StrepII, and Pfc_StrepII from the affinity chromatography purification step as described
193 previously [1].

194

195 **Results**

196 ***Purification of encapsulated ferritins from *H. ochraceum* and *P. furiosus****

197 The encapsulated ferritins from *H. ochraceum* and *P. furiosus* share 18 % amino acid sequence
198 identity with each other, and 58 % and 22 % with the *R. rubrum* EncFtn (respectively referred to as
199 Hoch_EncFtn, Pfc_EncFtn, and Rru_EncFtn herein). Residues shown to be in the ferroxidase centre
200 of the Rru_EncFtn protein are strictly conserved in the Hoch_EncFtn and Pfc_EncFtn proteins, with
201 secondary metal binding sites conserved in Hoch_EncFtn, but not in Pfc_EncFtn (Fig. S3).

202 To explore the structure and function of encapsulated ferritins from different species, we produced
203 examples of this protein family from *H. ochraceum* and *P. furiosus* as truncated variants, lacking the
204 C-terminal encapsulin localization sequence, by heterologous expression in *Escherichia coli*. The *H.*
205 *ochraceum* EncFtn was produced as a C-terminal His-tagged variant, C-terminal StrepII-tagged
206 variant, and an untagged variant comprising residues 1-98 of the native polypeptide. In *P. furiosus*
207 the encapsulated ferritin forms a single contiguous polypeptide with the encapsulin shell protein;
208 therefore, a truncated version with residues 1-99 encompassing just the EncFtn domain was
209 produced as both a C-terminal His-tagged variant, a C-terminal StrepII-tagged variant, and an
210 untagged variant. Purity and yield issues with untagged proteins were behind the rational of using
211 tagged-variants. His-tagged variants were produced for mass-spectrometry analysis, whereas C-
212 terminal StrepII-tagged variants were used in the enzymatic assay where the presence of the His-
213 tag could have interfered with metal binding and catalysis. Native untagged proteins were used for
214 protein crystallography as, after several attempts, only these variants produced crystals suitable for
215 X-ray diffraction. Average neutral masses were obtained for each homologue by liquid
216 chromatography mass spectrometry (Table S5). These all agree with the predicted masses of each
217 protein and revealed that some of the variants lacked full processing of the initiating methionine.

218 To interrogate the behaviour of the EncFtn homologues in solution, both the His-tagged and StrepII-
219 tagged variants were subjected to S200 size-exclusion chromatography, calibrated with standards
220 of known molecular weight, and followed by SDS-PAGE analysis (Fig. 1, Table S6, and Fig. S4).
221 Hoch_His eluted as three peaks of increasing area: a small peak at ~70 ml consistent with a decamer

oligomer; a peak at 81.6 ml consistent with a tetramer; and one at 87.6 ml corresponding to the dimer fraction. Pfc_His eluted as a single peak at 64 ml, which has a slightly larger apparent size than the decamer fraction of Rru_EncFtn (Fig. 1A). When subjected to SDS-PAGE the Hoch_His peak fractions were partially resistant to SDS and heat-induced denaturation, presenting bands at the approximate molecular weight of a monomer and dimer species (Fig. S4A); the Pfc_His peak fractions were almost fully resistant to SDS and heat denaturation with the majority of protein appearing as a band with an apparent molecular weight greater than that of a decamer, with a small proportion of monomer (Fig. S4B). Bands corresponding to dimer and monomer states were observed with Rru_His variant (Fig. S4C). The StreptII-tagged variants of the proteins behaved slightly differently in solution (Fig. 1B); Hoch_StreptII eluted as a monomer; while the Pfc_StreptII had a major decamer peak with two additional peaks consistent with higher-order aggregation, such as dimers of decamers and trimers of decamers. The Rru_StreptII protein eluted primarily as a decamer. Their appearance on SDS-PAGE gels was almost identical to the His-variants, with the appearance of some tetramer in the Pfc_StreptII fractions (Fig. S4D/E/F).

Native Mass spectrometry analysis

In order to further understand the differences seen in the solution-phase oligomerization states of the EncFtn homologues, native mass spectrometry was performed on the His-tagged variant of each homologue. As previously reported [1], the decameric assembly of iron-bound Rru_EncFtn can be successfully detected using this technique. Under native MS conditions (at pH 8.0), Rru_EncFtn displays a narrow charge state distribution consistent with the 22+ to 25+ charge state of the protein decamer (Fig. 2A, pink circles). In addition to the decamer, a minor species is observed which is consistent with the iron-free Rru_EncFtn monomer (+6 and +7) (Fig. 2A, blue circles).

In a similar manner to Rru_EncFtn, native MS analysis of Pfc_EncFtn demonstrates charge state distributions consistent with a decameric assembly (+23 to +26) (Fig. 2B, pink circles). Interestingly, the decameric charge state distribution is elongated (Fig. 2B, *) and low abundance (27+ to 31+) charge states are also observed. The elongated charge state distribution is only observed in Pfc_EncFtn, and we attribute its presence to the ability of the solvent-exposed affinity tag to readily protonate in solution. Similar to the observations from Rru_EncFtn, a charge state distribution

250 consistent with iron-free Pfc_EncFtn monomer (+5 to +17) is also observed (Fig. 2B, blue circles).
251 In contrast, native MS analysis of Hoch_EncFtn does not reveal a major decamer species. Instead
252 a series of oligomerization states are observed: the major species is a dimer (+9 to +12) (Fig. 2C,
253 green circles); in addition tetramer (+13 to +16), hexamer (17+ and 18+) and decamer (23+ to 25+),
254 and a small amount of monomer (+7 to +12) gas phase oligomerization states are all clearly
255 observed (Fig. 2C, purple circles, orange circles, pink circles, and blue circles respectively). This
256 observation is consistent with the multiple broad peaks obtained during size-exclusion
257 chromatography (Fig. 1).

258 These data suggest that, under our experimental conditions, multiple oligomeric assemblies of Hoch
259 protein exist in both the solution and gas phase. The observation of even-numbered oligomerization
260 states (i.e. dimer, tetramer and hexamer) suggests that one of the two dimer interfaces is partially
261 unstable, and the protein exists as an equilibrium of dimers and higher order multiples of dimers.

262 ***Crystal structures of Hoch and Pfc Encapsulated ferritins***

263 To explore the structure of the EncFtn homologues, crystals of native Hoch_EncFtn and Pfc_EncFtn
264 were produced by standard crystallization screening methods. Diffraction data were collected at
265 Diamond Light Source and the crystal structures of the Hoch_EncFtn and Pfc_EncFtn proteins were
266 determined by molecular replacement using a decamer of the Rru_EncFtn (PDB ID: 5DA5) as the
267 search model [1]. Data collection and refinement statistics are shown in Table 1.

268 The structure of Hoch_EncFtn was refined at 2.06 Å resolution and contained a decamer in the
269 asymmetric unit with visible electron density for residues 6 – 96 in each chain (Fig. 3A). Pfc_EncFtn
270 was refined at 2.03 Å resolution and contained three decamers in the asymmetric unit, with visible
271 electron density for residues 2-98 in each chain (Fig. 3B). The overall architecture of both structures
272 mirrors the annular decamer seen in the structure of Rru_EncFtn (Fig. 3C). The electrostatic surfaces
273 of these proteins display similar features to Rru_EncFtn, with negatively charged patches around
274 the circumference that correspond to the exterior metal binding sites seen on Rru_EncFtn, and a
275 negatively charged tunnel at the centre of the decamer corresponding to the interior metal binding
276 site (Fig. S5).

277 The monomers of Hoch_EncFtn and Pfc_EncFtn superimpose with an RMSD of 1.21 Å over 74 C α
278 atoms. Hoch_EncFtn superimposes on Rru_EncFtn with an RMSD of 0.47 Å over 91 C α atoms,
279 while Pfc_EncFtn superimposes with an RMSD of 1 Å over 71 C α atoms. While the Hoch_EncFtn
280 and Rru_EncFtn structures are almost identical, the Pfc_EncFtn structure presents several key
281 differences to these two proteins. At the N-terminus of Pfc_EncFtn, there is visible electron density
282 from Gly2, whereas the chains of both Hoch_EncFtn and Rru_EncFtn are not visible until residue
283 Gln6 and Ser7 respectively. The additional structured residues in Pfc_EncFtn form an extended loop
284 (Fig. 4), which lies in the central channel of the physiologically active decamer and forms a rigid
285 constriction when compared to the Hoch_EncFtn and Rru_EncFtn structures (Fig. 3B). The C-
286 terminal α 3 helix of Pfc_EncFtn has two additional turns when compared to the other structures and
287 is shifted by 25° relative to α 2 (Fig. 4B/C); this extends its interaction with the neighbouring dimer.
288 (Fig. 3B).

289 The main interaction surfaces that make up the decameric arrangement in the proteins correspond
290 to the ferroxidase centre dimer (FOC) and the non-ferroxidase dimer (non-FOC) interfaces (Fig.
291 3B/C). Analysis of the extent of these surfaces with PISA [25] gives a buried surface of 1186 Å² for
292 the Hoch_EncFtn FOC interface, with 8 hydrogen bonds and 16 salt bridges; and 1712 Å² in
293 Pfc_EncFtn, with 14 hydrogen bonds and 6 salt bridges (Fig S6). While Hoch_EncFtn buries roughly
294 the same surface area in its FOC interface as Rru_EncFtn FOC (1267 Å²), the latter has only 2
295 hydrogen bonds and 6 salt bridges; the additional stabilization of this interface in Hoch_EncFtn is
296 likely related to the environmental niche of *Haliangium ochraceum*, as proteins from halophilic
297 organisms tend to have an increased number of salt bridges when compared to those from
298 mesophiles [26]. The Pfc_EncFtn FOC interface has fourteen hydrogen bonds and six salt bridges;
299 this significant increase in hydrogen bonding over the Rru_EncFtn protein is likely to be a
300 consequence of the hyperthermophilic nature of *Pyrococcus furiosus*. The non-FOC interface for
301 Hoch_EncFtn buries 2338 Å², which is similar to the 2468 Å² buried in this region in Rru_EncFtn;
302 however, there are 18 hydrogen bonds compared to 16 in Rru_EncFtn, and 5 salt bridges compared
303 to 16 in Rru_EncFtn. These differences are due to a higher proportion of buried hydrophobic residues
304 in the Hoch_EncFtn interface. The non-FOC interface in the Pfc_EncFtn is less extensive than either

305 of the other two structures at 1793 Å² with 19 hydrogen bonds and 19 salt bridges. The extended
306 structured loop at the N-terminus and shifted α3 helix form one hydrogen bond each to the monomer
307 next to their partner in the FOC interface, to bury an additional 586 Å² of surface area (Fig S6). Taken
308 together, these two interfaces bury about the same surface area as the non-FOC interfaces of both
309 Rru_EncFtn and Hoch_EncFtn. The extended interaction surfaces in the Pfc_EncFtn potentially act
310 as a girdle around the decamer, further stabilizing it at high temperatures.

311 The residues in the iron binding site of the FOC interface are conserved in the Hoch_EncFtn and
312 Pfc_EncFtn structures (Fig. 5). The Pfc_EncFtn structure shows clear anomalous difference density
313 in data collected close to the iron edge at 1.74 Å (Fig. S7; therefore, a dinuclear iron centre was
314 modelled into the FOC of this structure (Fig. 5). The metal coordination in Pfc_EncFtn is identical to
315 that seen in Rru_EncFtn, with glutamic acid carboxyl oxygen to iron coordination distances of 2.1 Å,
316 and histidine nitrogen to iron distances of 2.2 Å. The electron density in the FOC interface of the
317 Hoch_EncFtn crystal does not contain any peaks or coordinated metal ions (Fig. S7). Given the
318 importance of the histidine residue (His64) for iron coordination [1] and the fact that the protein
319 crystallized in a buffer at pH 5.5, this histidine residue is likely to be around 70 % protonated and
320 would be unable to coordinate iron in this state, thus explaining the absence of iron in this site. In
321 the absence of iron in the Hoch_EncFtn structure, the side-chain of Glu31 is flipped 180° and is
322 within hydrogen bonding distance of Tyr38 from the partner chain, presumably stabilizing the apo-
323 form of this interface (Fig. 5A).

324 The secondary metal coordination sites seen in the structure of Rru_EncFtn are fully conserved in
325 Hoch_EncFtn and only partially so in Pfc_EncFtn. The metal binding site at the centre of the
326 decameric ring comprises Glu30/Glu33 in Hoch_EncFtn and Ala31/Asp34 in Pfc_EncFtn. Neither
327 structure has any coordinated metal ions in this site (Fig. 5B).

328 The side-chains of the glutamic acid residues (Glu31/Glu34 in Rru_EncFtn numbering) are shifted
329 when compared to those in Rru_EncFtn; this could be linked to the absence of a metal ion. The
330 external metal binding site of Hoch_EncFtn is identical to the Rru_EncFtn site, while the Pfc_EncFtn
331 has a glutamic acid in place of a histidine and alanine in place of a glutamic acid in this site.

332 Given the observation that a decameric form of Hoch_EncFtn was obtained in crystals at pH 5.5, the
333 influence of pH on protein oligomerization was investigated using native MS. Experiments were
334 performed in pH 5.5 ammonium acetate, and under these acidic conditions MS analysis reveals a
335 substantial increase in the abundance of the decameric species (21+ to 25+) (Fig. S8), similar to the
336 level seen for Pfc_EncFtn and Rru_EncFtn. The lower order oligomerization states, present at pH
337 8.0, are significantly reduced in abundance and only dimer (9+ and 10+) and tetramer (14+ and 15+)
338 minor species are observed (Fig. S8, green and purple circles respectively). Taken together, our
339 native MS observations suggest that a stable Hoch EncFtn dimer is readily formed irrespective of
340 pH; and under acidic conditions, Hoch_EncFtn dimers favour assembly into the higher order
341 pentamer-of-dimers annular structure which is characteristic of this class of protein.

342 ***Ferroxidase activity***

343 Given the absolute conservation of the FOC residues in Hoch_EncFtn, Pfc_EncFtn and Rru_EncFtn,
344 the ferroxidase activity of the EncFtn homologues was tested to determine if they were indeed active
345 as ferroxidase enzymes. Encapsulated ferritin StrepII-tagged variants were assayed for their
346 ferroxidase activity by following progress curves for iron oxidation at 315 nm at 20 °C. Each of the
347 proteins displayed similar activity profiles, with some small differences in the shape of the progress
348 curves. Hoch_EncFtn exhibits a higher initial rate than the other homologues (Fig. 6). Overall these
349 data confirm the ferroxidase activity of the EncFtn family across different species from distinct
350 environmental niches.

351 The metal content of the purified protein fractions used for enzymatic assays was determined by
352 inductively coupled plasma mass spectrometry (Table S7). Iron levels determined in StrepII-tagged
353 monomeric Hoch_EncFtn variants and StrepII-tagged decameric Pfc_EncFtn and Rru_EncFtn
354 variants show an iron to protein ratio consistent with 40-80 % occupancy of the ferroxidase centre,
355 assuming all of the iron is located within this site. A ~50 % occupancy of the ferroxidase centre was
356 also observed with the His-tagged EncFtn variants which were used in the mass-spectrometry
357 analysis.

358 Significant amounts of zinc were copurified with all protein samples in this study, with varying levels
359 detected in the forms with different tags. Zinc is known to strongly inhibit the ferroxidase activity of

360 ferritin family proteins via competitive binding to the ferroxidase centre [27]. Given the structural
361 differences between encapsulated ferritins and the classical ferritins, and the differences in
362 secondary metal-binding sites displayed by Pfc_EncFtn, the inhibitory effect of zinc on the EncFtn
363 homologues was tested by performing the ferroxidase assays in the presence of increasing
364 concentrations of zinc. The results show that increasing zinc concentrations lead to a decrease in
365 the slope and final level of ferroxidase progress curves for all of the EncFtn variants, with a maximum
366 inhibition seen with ~ 40-100 μ M Zn (Fig. S9). These data were fitted using a nonlinear regression
367 with a dose-response model with three parameters, where the response (zero-subtracted end-point
368 absorbance at 315 nm) was the average of three replicates per condition (Fig. 7). The calculated
369 IC₅₀ values for zinc inhibition of the three EncFtn variants (Table S8) show significant differences,
370 with the Rru_EncFtn showing the lowest, and Hoch_EncFtn the highest IC₅₀ values. The lower
371 susceptibility of the Hoch_EncFtn to zinc dependent inhibition could be a consequence of a higher
372 level of ferroxidase activity, or structural differences that influence metal binding and discrimination.

373

374

375

376

377 Discussion

378 The recently published structural and functional analysis of the *R. rubrum* encapsulated ferritin
379 system presented a new functional organization for iron mineralization by ferritin-like proteins, with
380 the four-helix bundle ferritin-like fold formed through the interaction of EncFtn subunits to form a
381 functional ferroxidase centre [1]. The open decameric structure of the EncFtn protein is not
382 competent to store iron in mineral form; instead, the interaction with, and sequestration within, the
383 encapsulin nanocage provides a functional and high-capacity iron storage system [3,4]. To
384 understand whether the structural organization of the EncFtn family is conserved across
385 microorganisms with different environmental niches and distinct encapsulin geometries, we
386 determined the structure and biochemical properties of EncFtn proteins from *H. ochraceum* and *P.*
387 *furiosus*.

388 *P. furiosus* is a hyperthermophilic Euryarchaeota and its encapsulin was the first to be characterized;
389 however, it was initially mis-annotated as a non-functional virus-like particle [13]. The *P. furiosus*
390 encapsulin forms a contiguous polypeptide chain with an N-terminal EncFtn domain appended to it
391 and assembles into a 180 subunit T=3 capsid. This archaeal arrangement is distinct to the bacterial
392 EncFtn/encapsulin systems, which are usually encoded in a two-gene operon with the EncFtn
393 upstream of the encapsulin, and with a short C-terminal encapsulation sequence peptide appended
394 to the encoded EncFtn protein [5, 10]. It is not clear whether the genomic arrangement of the bacterial
395 EncFtn/encapsulin systems arose separately, or by horizontal gene transfer from archaea followed
396 by mutation of the single-reading frame into two, along with the mutation of the T=3 form of the
397 encapsulin to the T=1 form found in the bacterial EncFtn encapsulins.

398 The published crystal structure of the *P. furiosus* encapsulin lacks any electron density for
399 the EncFtn domain, implying that this domain is mobile within the encapsulin nanocage even though
400 it is contiguous with and tethered to the encapsulin protein [13]. Our analysis focused on the isolated
401 *P. furiosus* EncFtn domain, which forms a decamer in solution, the gas phase, and in crystals. This
402 domain is partially resistant to thermal and SDS induced denaturation, which is in accord with the
403 extreme temperatures endured by the host organism in its volcanic niche.

404 The current model for the organization of bacterial EncFtn proteins within encapsulin nanocages
405 places the decamers at the pentameric vertices of the T=1 capsid [1,4] with the encapsulation
406 sequences of five subunits captured by clefts on the interior surface of the penton of the encapsulin
407 shell. The encapsulation sequences of the other five subunits in the decamer are disengaged and
408 free within the interior of the capsid. No evidence is available on the strength of the interaction
409 between the capsid and the EncFtn protein; however, the presence of clear electron density for some
410 of the encapsulation sequence in the *T. maritima* encapsulin structure implies that the interaction is
411 relatively stable, and this is enhanced by an avidity mechanism with multiple encapsulation
412 sequences engaged by subunits at the pentameric vertex [4]. In the archaeal systems the EncFtn
413 and encapsulin domains are a contiguous polypeptide, with the EncFtn domain tethered to the
414 interior of the capsid. The T=3 geometry of the *P. furiosus* encapsulin has 180 subunits, with 12
415 penton units and 20 hexons. Given the structural and biochemical conservation of the decameric
416 EncFtn protein, it is likely that this arrangement is found within the T=3 as well as T=1 capsids. It is
417 not clear how the decamer could be formed from tethered subunits unless the EncFtn domains found
418 in hexons have enough flexibility in the linker between domains to engage with partners in adjacent
419 pentons. With full engagement at the pentons, this would leave 60 'free' EncFtn domains within the
420 capsid. This observation, coupled with our solution and gas phase experiments, indicates that the
421 quaternary structure of EncFtn proteins is dynamic and that they can exist in equilibrium between
422 monomers/dimers and higher order multiples of dimers.

423 The dynamic nature of EncFtn proteins is highlighted in our solution and gas phase analyses
424 of the *H. ochraceum* EncFtn. Despite high sequence identity and the conservation of key residues
425 between it and the *R. rubrum* EncFtn, this protein is less prone to multimerization in solution and
426 displays a greater range of oligomerization intermediates than both the *R. rubrum* and *P. furiosus*
427 EncFtn proteins in the gas phase. The presence of the conserved EncFtn decamer quaternary
428 structure in the crystal highlights the conservation of this architecture. The absence of metal ions in
429 the crystal structure, which was formed at pH 5.5, indicated that the quaternary structure can be
430 induced by both metal binding, as was shown in solution for the *R. rubrum* EncFtn [1], and changes
431 in pH, presumably through the protonation of the conserved histidine at low pH and the formation of
432 stabilizing hydrogen bonds by residues normally involved in the formation of the FOC.

433 Analysis of the structure and sequence of the *H. ochraceum* EncFtn indicates that the dimerization
434 interfaces are less extensive than the *R. rubrum* EncFtn interfaces and are discontinuous. This leads
435 to lower binding energies for both of the interfaces when compared to both *R. rubrum* and *P. furiosus*,
436 and this could explain the differences in stability seen in solution and the gas phase.

437 We show here that the three proteins in this study exhibit comparable ferroxidase activities. This
438 indicates that they were purified in a functional state. Previous reports show that ferritins are
439 susceptible to inhibition by Zn(II) ions [27], which is also the case for the EncFtn family as
440 demonstrated in this study. In the experimental conditions used in our study, the *H. ochraceum*
441 EncFtn was slightly more active than the other proteins and less susceptible to inhibition by zinc.
442 This may be a consequence of the more dynamic nature of this homologue, as seen in solution and
443 the gas phase. The precise mode of catalysis for ferritins is a subject of some debate and key
444 questions as to whether the iron ions engaged within the ferroxidase centre are labile, or act as a
445 stable prosthetic centre; and whether the two iron ions move in concert are the subject of some
446 controversies in the field [28,29]. Our study does not aim to address these controversies, but we do
447 note that the location of the conserved FOC and secondary metal binding sites at a dimer interface
448 and the dynamic nature of EncFtn oligomerization may indicate a distinct mechanism of iron
449 oxidation and transfer to minerals when compared to the classical ferritins, thus adding a new level
450 of complexity and debate to the field. It must also be noted that the activity of EncFtn proteins occurs
451 within the privileged environment of an encapsulin shell, which adds an additional level of complexity
452 to the study of their catalysis.

453 Analysis of the sequence alignment (Fig. S3) highlights the absence of conserved residues found in
454 the putative metal ion entry site found in the other EncFtn homologues. Our observation that Pfc
455 EncFtn displays ferroxidase activity highlights that conservation of this site is not a prerequisite for
456 catalysis. However, it is clear that Pfc_EncFtn has the lowest enzymatic activity of the three
457 homologues, it may be that the acidic residues found in this location attract iron ions and channel
458 them to the FOC. Their absence in Pfc_EncFtn implies that metal ions reach its FOC simply by
459 diffusion, resulting in a slower Fe(II)/Fe(III) turn-over and hence a reduction in enzyme activity. It
460 would be interesting to apply a mutagenesis approach to further explore the role of these proposed

461 entry site residues on the ferroxidase activity. The modest catalytic activity displayed by Pfc_EncFtn
462 could also be interpreted by considering that *P. furiosus* achieves optimal growth at ~ 100 °C,
463 whereas enzymatic experiments were conducted at room temperature to allow the comparison of
464 activities.

465 Further study will shed light on the role of the different dimerization interfaces on the stability of the
466 EncFtn decamer; and the role of the secondary metal binding sites on catalysis, metal selectivity,
467 and catalytic inhibition by competing metal ions.

468

469 **Author Contributions**

470 DH, JMW and DC conceived the study. DH produced the native and His-tagged constructs used in
471 the study. LRT produced the DNA parts and assembled the StrepII-tagged variants of the EncFtn
472 proteins. DH, CP, JR, ZM and JMW produced recombinant proteins used in the study. DH and JMW
473 determined and refined the crystal structures. CP performed biochemical assays shown in Figures
474 6/7/S9. JR and DC performed mass spectrometry experiments shown in Figures 2 and S8. CLM
475 provided technical assistance and contributed to data collection for MS experiments. KJW and ET
476 performed ICP-MS experiments shown in Table S7. All authors contributed to data analysis and
477 preparation of the manuscript.

478 **Funding**

479 This work was supported a Royal Society Research Grant awarded to JMW (RG130585) and a
480 BBSRC New Investigator Grant to JMW and DJC (BB/N005570/1). JMW is funded by Newcastle
481 University. DJC and JR are funded by the University of Edinburgh. JR is funded by a BBSRC EastBio
482 DTP studentship (BB/M010996/1). DH was funded by the China Scholarship Council. LRT was
483 funded by a BBSRC EastBio DTP Studentship (BB/M010996/1). KJW and ET were funded by the
484 Wellcome Trust and Royal Society through a Sir Henry Dale Fellowship awarded to KJW
485 (098375/Z/12/Z).

486 **Competing Interests**

487 The authors declare that there are no competing interests.

488 **Acknowledgements**

489 The authors would like to thank Diamond Light Source for beamtime (proposal mx9487), and the
490 staff of beamlines I04 and I24 for assistance with crystal testing and data collection.

491 We would like to thank Prof Dominic Campopiano and Dr Elisabeth Lowe for their critical reading of
492 this manuscript and helpful discussions.

493

494

495 **References**

- 496 1 He, D., Hughes, S., Vanden-Hehir, S., Georgiev, A., Altenbach, K., Tarrant, E., Mackay, C. L.
497 L., Waldron, K. J. K. J., Clarke, D. J. D. J. and Marles-Wright, J. (2016) Structural
498 characterization of encapsulated ferritin provides insight into iron storage in bacterial
499 nanocompartments. *Elife* **5**, e18972.
- 500 2 Andrews, S. C. (2010) The Ferritin-like superfamily: Evolution of the biological iron storeman
501 from a rubrerythrin-like ancestor. *Biochim. Biophys. Acta*, Elsevier B.V. **1800**, 691–705.
- 502 3 McHugh, C. A., Fontana, J., Nemecek, D., Cheng, N., Aksyuk, A. A., Heymann, J. B., Winkler,
503 D. C., Lam, A. S., Wall, J. S., Steven, A. C., et al. (2014) A virus capsid - like
504 nanocompartment that stores iron and protects bacteria from oxidative stress. *EMBO J.*,
505 EMBO Press **33**, 1896–1911.
- 506 4 Sutter, M., Boehringer, D., Gutmann, S., Günther, S., Prangishvili, D., Loessner, M. J., Stetter,
507 K. O., Weber-Ban, E. and Ban, N. (2008) Structural basis of enzyme encapsulation into a
508 bacterial nanocompartment. *Nat. Struct. Mol. Biol.*, Nature Publishing Group **15**, 939–947.
- 509 5 Giessen, T. W. and Silver, P. A. (2017) Widespread distribution of encapsulin
510 nanocompartments reveals functional diversity. *Nat. Microbiol.*, Nature Publishing Group **2**,
511 17029.
- 512 6 Crow, A., Lawson, T. L., Lewin, A., Moore, G. R. and Le Brun, N. E. (2009) Structural basis
513 for iron mineralization by bacterioferritin. *J. Am. Chem. Soc.*, American Chemical Society **131**,
514 6808–13.
- 515 7 Bakker, G. R. and Boyer, R. F. (1986) Iron incorporation into apoferritin. The role of apoferritin
516 as a ferroxidase. *J. Biol. Chem.* **261**, 13182–13185.
- 517 8 Bradley, J. M., Moore, G. R. and Le Brun, N. E. (2014) Mechanisms of iron mineralization in
518 ferritins: one size does not fit all. *J. Biol. Inorg. Chem.* **19**, 775–85.
- 519 9 Chasteen, N. D. and Harrison, P. M. (1999) Mineralization in ferritin: an efficient means of iron
520 storage. *J. Struct. Biol.* **126**, 182–94.
- 521 10 Sutter, M., Boehringer, D., Gutmann, S., Günther, S., Prangishvili, D., Loessner, M. J., Stetter,

522 K. O., Weber-Ban, E. and Ban, N. (2008) Structural basis of enzyme encapsulation into a
523 bacterial nanocompartment. *Nat. Struct. Mol. Biol.* **15**, 939–947.

524 11 Snijder, J., Kononova, O., Barbu, I. M., Uetrecht, C., Rurup, W. F., Burnley, R. J., Koay, M. S.
525 T., Cornelissen, J. J. L. M., Roos, W. H., Barsegov, V., et al. (2016) Assembly and Mechanical
526 Properties of the Cargo-Free and Cargo-Loaded Bacterial Nanocompartment Encapsulin.
527 *Biomacromolecules* **17**, 2522–9.

528 12 Rurup, W. F., Snijder, J., Koay, M. S. T., Heck, A. J. R. and Cornelissen, J. J. L. M. (2014)
529 Self-sorting of foreign proteins in a bacterial nanocompartment. *J. Am. Chem. Soc., American*
530 *Chemical Society* **136**, 3828–32.

531 13 Akita, F., Chong, K. T., Tanaka, H., Yamashita, E., Miyazaki, N., Nakaishi, Y., Suzuki, M.,
532 Namba, K., Ono, Y., Tsukihara, T., et al. (2007) The crystal structure of a virus-like particle
533 from the hyperthermophilic archaeon *Pyrococcus furiosus* provides insight into the evolution
534 of viruses. *J. Mol. Biol.* **368**, 1469–83.

535 14 Iverson, S. V., Haddock, T. L., Beal, J. and Densmore, D. M. (2016) CIDAR MoClo: Improved
536 MoClo Assembly Standard and New *E. coli* Part Library Enable Rapid Combinatorial Design
537 for Synthetic and Traditional Biology. *ACS Synth. Biol., American Chemical Society* **5**, 99–
538 103.

539 15 Kabsch, W. (2010) Integration, scaling, space-group assignment and post-refinement. *Acta*
540 *Crystallogr. Sect. D Biol. Crystallogr., International Union of Crystallography* **66**, 133–144.

541 16 Evans, P. R. (2011) An introduction to data reduction: space-group determination, scaling and
542 intensity statistics. *Acta Crystallogr. D. Biol. Crystallogr.* **67**, 282–92.

543 17 Evans, P. (2006) Scaling and assessment of data quality. In *Acta Crystallographica Section*
544 *D: Biological Crystallography*, pp 72–82, International Union of Crystallography.

545 18 Stein, N. (2008) CHAINSAW: A program for mutating pdb files used as templates in molecular
546 replacement. *J. Appl. Crystallogr.* **41**, 641–643.

547 19 Terwilliger, T. C., Grosse-Kunstleve, R. W., Afonine, P. V., Moriarty, N. W., Zwart, P. H., Hung,
548 L. W., Read, R. J. and Adams, P. D. (2007) Iterative model building, structure refinement and

549 density modification with the PHENIX AutoBuild wizard. *Acta Crystallogr. Sect. D Biol.*
550 *Crystallogr.*, International Union of Crystallography **64**, 61–69.

551 20 Afonine, P. V., Grosse-Kunstleve, R. W., Echols, N., Headd, J. J., Moriarty, N. W.,
552 Mustyakimov, M., Terwilliger, T. C., Urzhumtsev, A., Zwart, P. H. and Adams, P. D. (2012)
553 Towards automated crystallographic structure refinement with phenix.refine. *Acta Crystallogr.*
554 *Sect. D Biol. Crystallogr.*, International Union of Crystallography **68**, 352–367.

555 21 Emsley, P., Lohkamp, B., Scott, W. G. and Cowtan, K. (2010) Features and development of
556 Coot. *Acta Crystallogr. D. Biol. Crystallogr.* **66**, 486–501.

557 22 Chen, V. B., Arendall, W. B., Headd, J. J., Keedy, D. A., Immormino, R. M., Kapral, G. J.,
558 Murray, L. W., Richardson, J. S. and Richardson, D. C. (2010) MolProbity: all-atom structure
559 validation for macromolecular crystallography. *Acta Crystallogr. D. Biol. Crystallogr.* **66**, 12–
560 21.

561 23 Sievers, F. and Higgins, D. G. (2014) Clustal Omega, accurate alignment of very large
562 numbers of sequences. *Methods Mol. Biol.* **1079**, 105–16.

563 24 Gouet, P., Robert, X. and Courcelle, E. (2003) ESPript/ENDscript: Extracting and rendering
564 sequence and 3D information from atomic structures of proteins. *Nucleic Acids Res.* **31**,
565 3320–3.

566 25 Krissinel, E. and Henrick, K. (2007) Inference of macromolecular assemblies from crystalline
567 state. *J. Mol. Biol.* **372**, 774–97.

568 26 DasSarma, S. and DasSarma, P. (2015) Halophiles and their enzymes: negativity put to good
569 use. *Curr. Opin. Microbiol.* **25**, 120–126.

570 27 Pfaffen, S., Abdulqadir, R., Le Brun, N. E. and Murphy, M. E. P. (2013) Mechanism of ferrous
571 iron binding and oxidation by ferritin from a pennate diatom. *J. Biol. Chem.* **288**, 14917–25.

572 28 Ebrahimi, K., Eckhard, B., Hagedoorn, P. and Hagen, W. (2012) The catalytic center of ferritin
573 regulates iron storage via Fe (II)-Fe (III) displacement. *Nat. Chem. Biol.* **8**, 941–948.

574 29 Hagen, W. R., Hagedoorn, P.-L. and Honarmand Ebrahimi, K. (2017) The workings of ferritin:

575 a crossroad of opinions. Metallomics, The Royal Society of Chemistry **9**, 595–605.

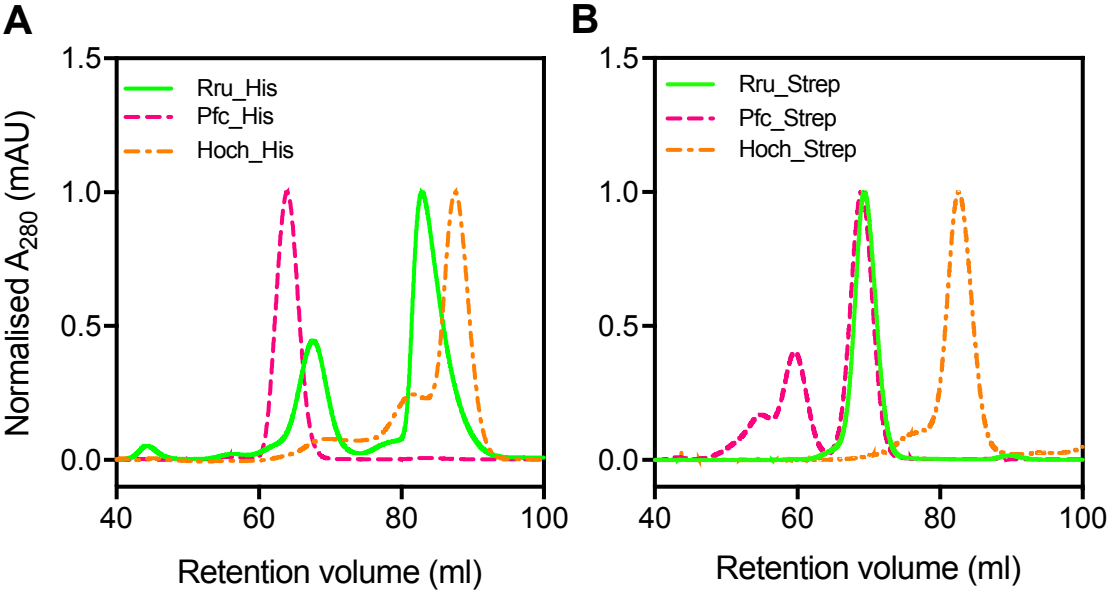
576

577

579 Table 1. X-ray diffraction data collection and refinement statistics.

	Hoch_EncFtn	Pfc_EncFtn*
Data collection		
Wavelength (Å)	1.72	1.74
Resolution range (Å)	47.82 - 2.06 (2.13 - 2.06)	47.19 - 2.03 (2.1 - 2.03)
Space group	C 1 2 1	P 1 2 1 1
Unit cell (Å)	91.63, 92.65, 119.29	99.85, 110.06, 136.27
β (°)	106.94	91.22
Total reflections	30,0549 (27,242)	1,226,338 (112,156)
Unique reflections	57,293 (5,570)	374,905 (36,076)
Multiplicity	5.2 (4.9)	3.3 (3.0)
Completeness (%)	96.3 (94.1)	97.0 (95.4)
Mean I/sigma(I)	10.16 (2.37)	10.48 (4.02)
Wilson B-factor (Å²)	31.7	22.8
R_{merge} (%)	9.4 (59.6)	8.0 (36.3)
R_{meas} (%)	10.5 (66.7)	9.5 (44.1)
R_{pim} (%)	4.4 (29.2)	5.2 (24.7)
CC_{1/2} (%)	100 (99.9)	99.5 (90.2)
CC* (%)	100 (97.6)	100 (97.4)
Image DOI	10.5281/zenodo.322743	10.5281/zenodo.344797
Refinement		
Reflections used in refinement	57,082 (5,563)	365,581 (36,036)
Reflections used for R-free	2,765 (284)	17,934 (1697)
Rwork (%)	20.1 (29.5)	17.5 (22.3)
Rfree (%)	24.5 (34.5)	20.2 (24.5)
CC(work) (%)	96.4 (92.6)	96.7 (92.3)
CC(free) (%)	93.6 (85.1)	95.3 (90.3)
Non-hydrogen atoms	7,819	25,735
macromolecules	7,650	23,691
ligands	1	30
Water	168	2,014
Protein residues	916	2,922
RMS(bonds) (Å)	0.003	0.002
RMS(angles) (°)	0.46	0.44
Ramachandran		
favoured (%)	98.7	99.9
allowed (%)	1.3	0.10
outliers (%)	0.00	0.00
Rotamer outliers (%)	0.96	0.39
Clashscore	1.20	1.15
Average B-factor (Å²)	44.6	29.0
macromolecules	44.6	28.3
ligands	34.7	19.7
solvent	43.7	36.7
PDB ID	5N5F	5N5E

580 *Anomalous pairs were counted separately for Pfc_EncFtn, as this model was refined against the split
581 anomalous data. Statistics for the highest-resolution shell are shown in parentheses.



584

585 **Figure 1. Purification of recombinant *R. rubrum*, *H. ochraceum*, and *P. furiosus* EncFtn**

586 **proteins.** A, Recombinant His-tagged Hoch_His, Pfc_His, and Rru_His proteins were purified by

587 nickel NTA-affinity chromatography and subjected to analytical size-exclusion chromatography

588 using a Superdex 200 16/60 column (GE Healthcare) equilibrated with 50 mM Tris-HCl, pH 8.0,

589 150 mM NaCl. The peaks near 70 ml correspond to an estimated molecular weight of >130 kDa

590 when compared to calibration standards, consistent with oligomerisation states equal or greater

591 than decameric. The Hoch_His at around 80 ml corresponds to the 50 kDa tetramer and the peaks

592 near 88 ml correspond to the 31 kDa dimer compared to the standards. B, Recombinant Strep-

593 tagged Hoch_StrepII, Pfc_StrepII, and Rru_StrepII proteins were purified by Strep-Trap column HP

594 (GE Healthcare). Purified samples were applied to a Superdex 200 16/60 column (GE Healthcare)

595 equilibrated with 50 mM Tris-HCl, pH 8.0, 150 mM NaCl in order to observe oligomerization state

596 in solution. Rru_StrepII elutes primarily at ~ 70 ml, corresponding to the decamer size. Pfc_StrepII

597 peaks can be found around 60 ml (~ 24-mer) and at 70 ml (12-mer), whereas Hoch_StrepII elutes

598 at ~ 83 ml (4-mer). Elution volumes and corresponding oligomerisation states are summarised in

599 Table S6. DOI: 10.6084/m9.figshare.7105907

600

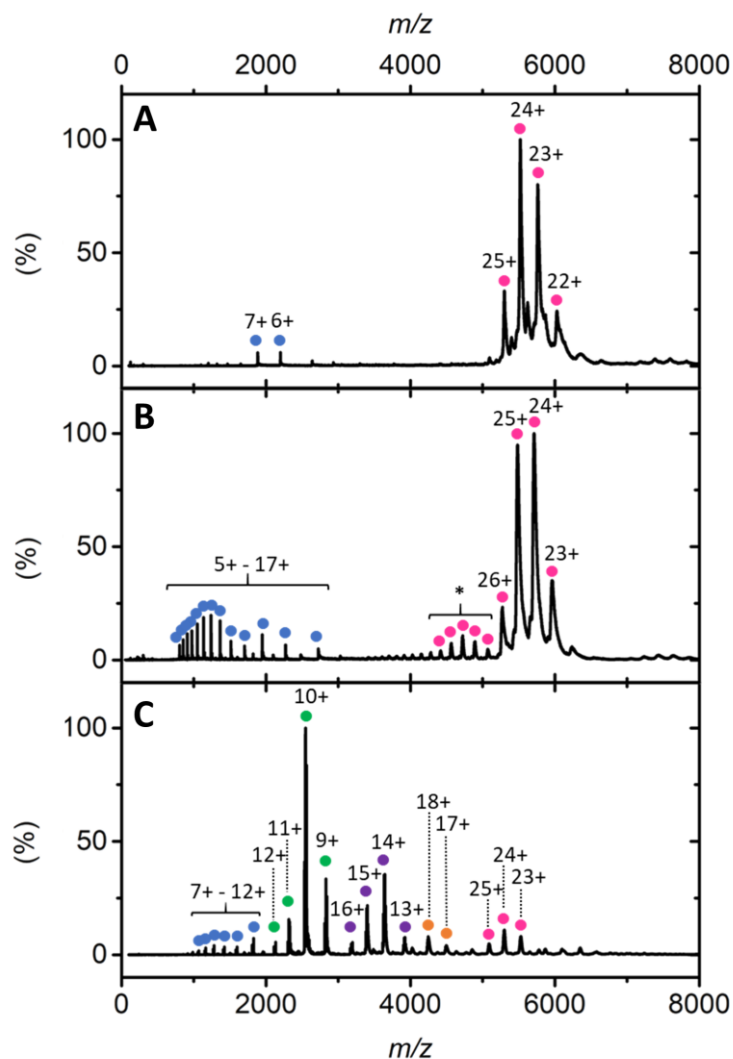


Figure 2. Native mass spectrometry of encapsulated ferritin homologues. Native nanoelectrospray ionization (nESI) mass spectrometry of encapsulated ferritin homologues acquired in 100 mM ammonium acetate (pH 8.0). **A:** nESI spectrum of Rru_EncFtn consistent with decameric assembly. The decameric charge state distribution is represented with pink circles and peaks correspond to 22+ to 25+ charge states. Two minor monomer charge states (blue circles, 6+ and 7+ charge states) are also observed. **B:** Native spectrum of Pfc_EncFtn. Decamer charge states (23+ to 31+) are highlighted with pink circles and monomer charge states (5+ to 17+) are highlighted by blue circles. * denotes the extended charge state observed. **C:** nESI spectrum of Hoch_EncFtn with gas phase oligomerization stressed with coloured circles. Monomer shown as blue; dimer as green; tetramer as purple; hexamer as yellow and decamer as pink.

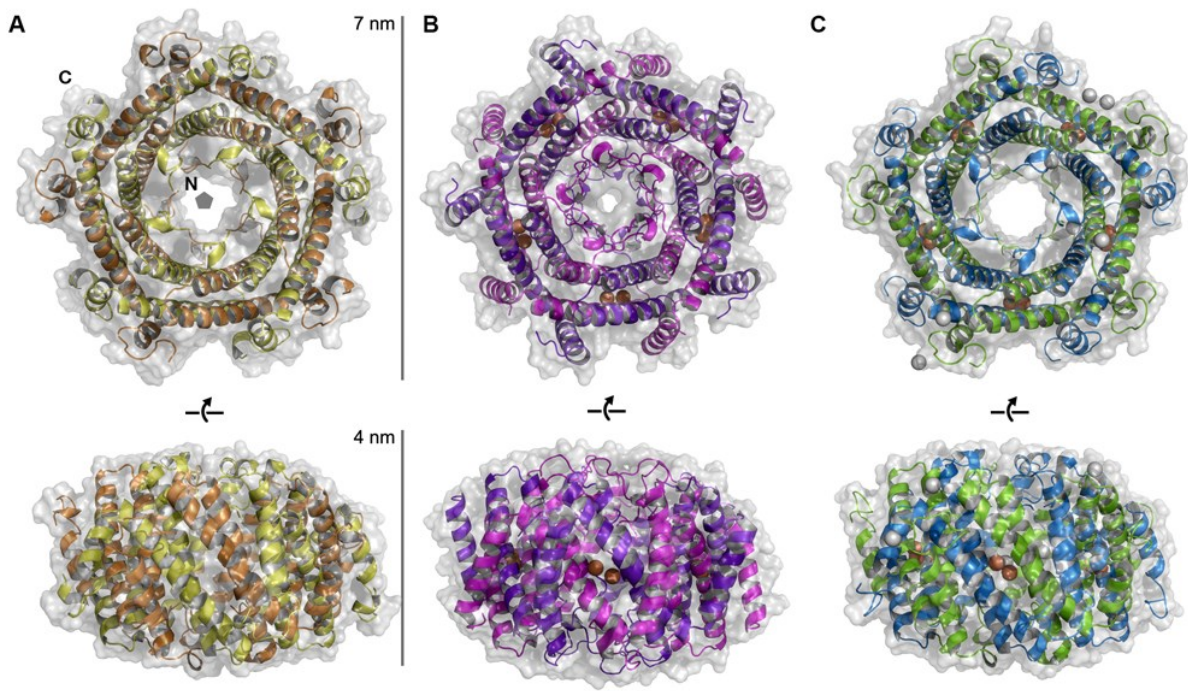
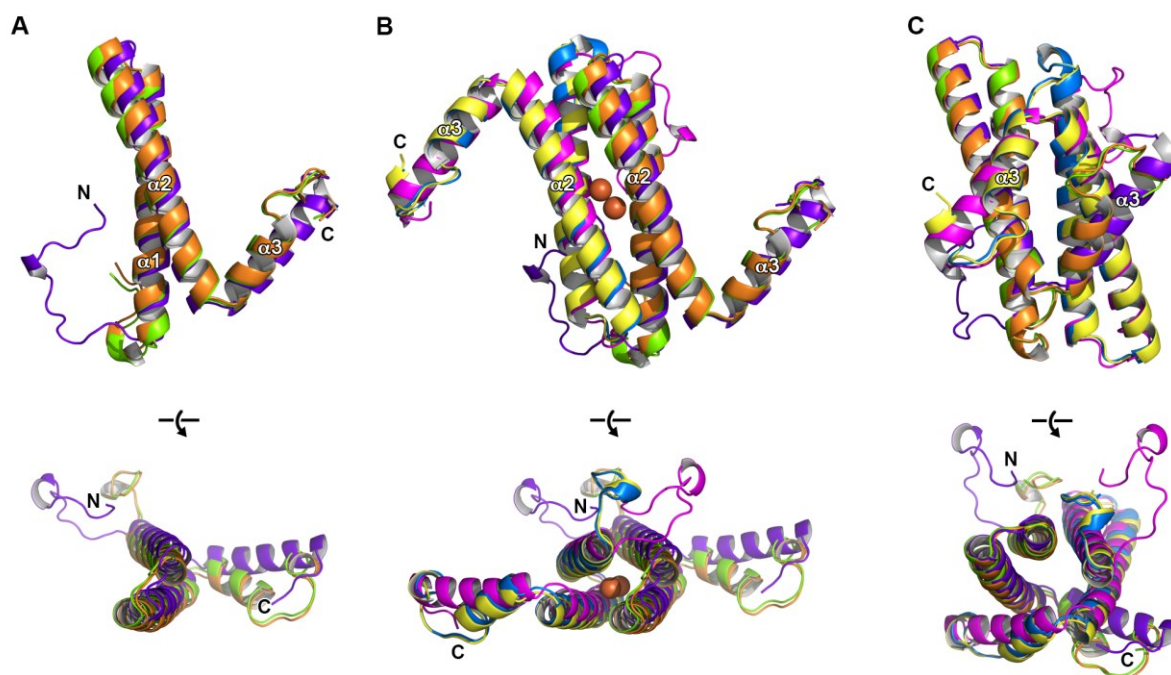


Figure 3. Encapsulated ferritins from *Haliangium ochraceum* and *Pyrococcus furiosus* form annular decamers. The annular decameric architecture of the encapsulated ferritins from *Haliangium ochraceum*, A, and *Pyrococcus furiosus*, B, are shown as transparent solvent accessible surfaces over secondary structure cartoons. The published structure of the *Rhodospirillum rubrum* encapsulated ferritin is shown for comparison, C (PDB ID: 5DA5) [1]. Bound metal ions are shown as spheres: iron ions are depicted in orange, and calcium ions in grey. The positions of the N- and C-termini of the protein chains and five-fold symmetry axis are highlighted in panel A.



623

624 **Figure 4. Crystal structures of encapsulated ferritins from *Haliangium ochraceum* and**

625 ***Pyrococcus furiosus*. Secondary structure cartoon depictions of the structures of the protomers**

626 **and dimers found in the crystal structures of the Hoch_EncFtn and Pfc_EncFtn encapsulated**

627 **ferritins. A, orthogonal views of the protomers: Hoch_EncFtn shown in orange; Pfc_EncFtn in**

628 **purple; and Rru_EncFtn in green for comparison (PDB ID: 5DA5) [1]. B, orthogonal views of the**

629 **ferroxidase centre dimer. Iron ions present in the Pfc_EncFtn dimer are shown as orange spheres.**

630 **No metal ions were present in the Hoch_EncFtn structure. Hoch_EncFtn is shown in**

631 **orange/yellow; Pfc_EncFtn in purple/pink; and Rru_EncFtn in green/blue. C, orthogonal views of**

632 **the non-FOC dimer, depicted as in B.**

633

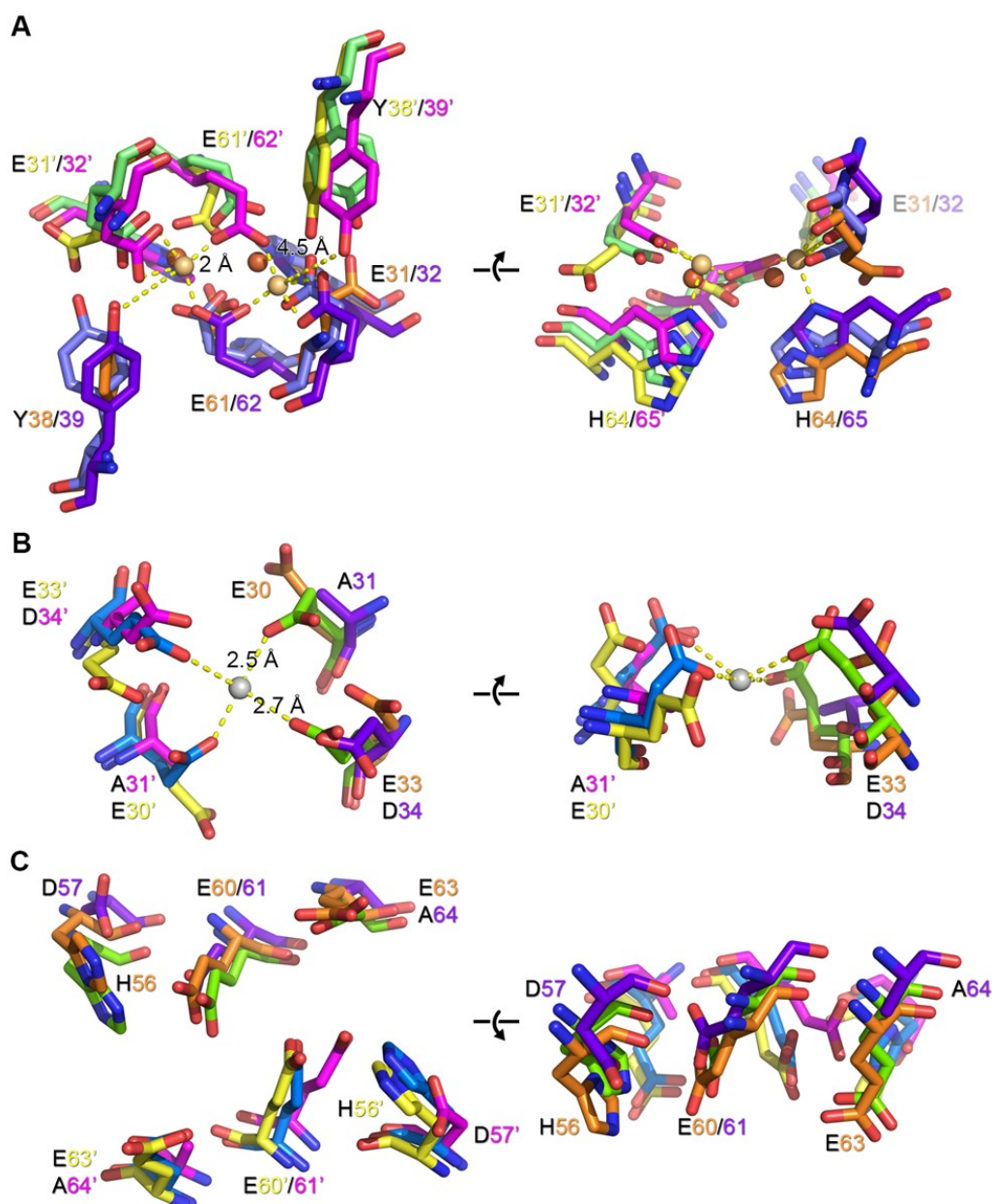
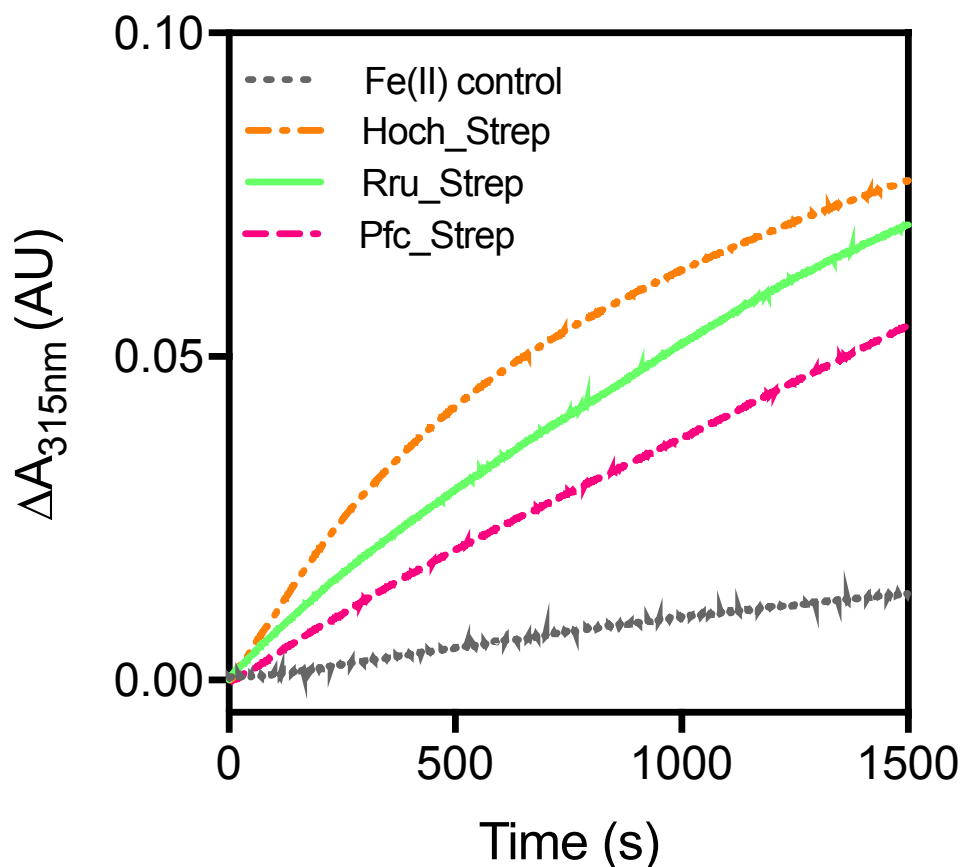


Figure 5. Ferroxidase centre and putative metal binding sites of encapsulated ferritins.

Orthogonal views of the ferroxidase centre (A) and putative secondary metal binding sites (B/C) of Hoch_EncFtn (yellow/orange) and Pfc_EncFtn (pink/purple) compared to Rru_EncFtn (PDB ID: 5DA5) [1] (blue/green). A, conserved ferroxidase centre residues are numbered for Hoch_EncFtn and Pfc_EncFtn. Iron ions found in the Pfc_EncFtn FOC are shown as gold spheres with coordination distances to side chain atoms shown. The positions of the iron ions in the Rru_EncFtn structure are shown as orange spheres. B, residue conservation in the site occupied by calcium in the Rru_EncFtn structure (grey sphere, with coordination distances). C, conserved residues on the outer surface of the encapsulated ferritin surface, located 10 Å from the FOC.

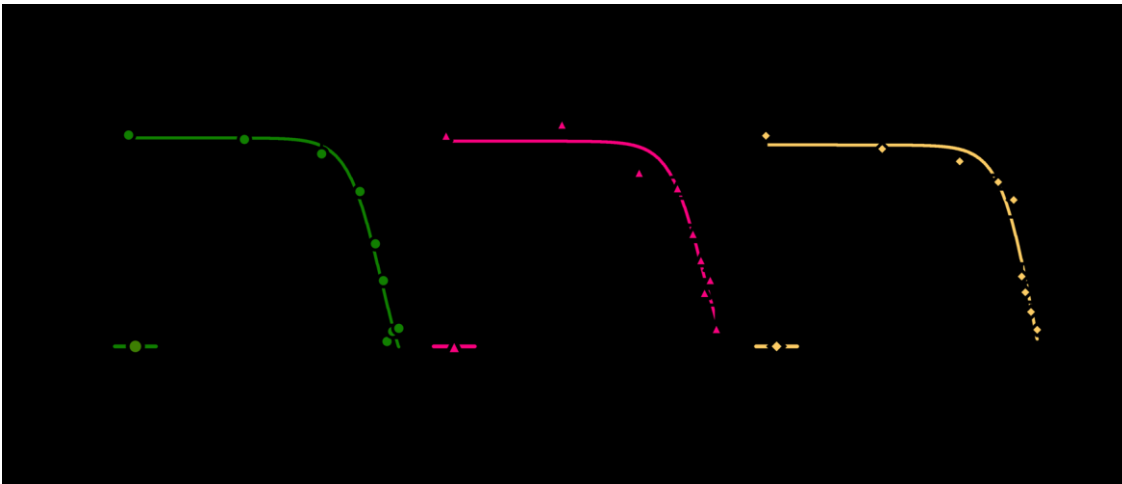


644

645 **Figure 6. Ferroxidase activity of encapsulated ferritins.** Hoch_StrepII(dotdash orange line),
 646 Pfc_StrepII(dashed pink line), and Rru_StrepII(solid green line) (10 μ M monomer) were incubated
 647 with 50 μ M $\text{FeSO}_4 \cdot 7\text{H}_2\text{O}$ (10 times molar equivalent Fe^{2+} per FOC) and progress curves of the
 648 oxidation of Fe^{2+} to Fe^{3+} was monitored at 315 nm. The background oxidation of iron at 50 μ M in
 649 enzyme-free control is shown for reference (dotted grey line). Solid lines represent the average (n
 650 = 3) of technical replicates, shaded areas represent standard deviation from the mean.

651 DOI: 10.6084/m9.figshare.7718879

652



653

654

655

656

657

658

659

660

661

662

663

Figure 7. The ferroxidase activity of encapsulated ferritins is inhibited by zinc. A, B, C, Non-linear fit of ferroxidase activities of Strep-tagged proteins inhibited by varying concentrations of Zn(II) by GraphPad software using a Dose-Response (log(inhibitor) vs. response (three parameters) equation. Response used in this analysis is the average of three technical replicates per condition. Data shown were recorded after 1500 seconds from the start of the assay. IC_{50} and $\log IC_{50}$ have been calculated for each protein (Table S8).

DOI:

10.6084/m9.figshare.7718879